



HAL
open science

Carbon-Binder Migration: A Three-Dimensional Drying Model for Lithium-ion Battery Electrodes

Teo Lombardo, Alain C. Ngandjong, Amal Belhcen, Alejandro A. Franco

► **To cite this version:**

Teo Lombardo, Alain C. Ngandjong, Amal Belhcen, Alejandro A. Franco. Carbon-Binder Migration: A Three-Dimensional Drying Model for Lithium-ion Battery Electrodes. *Energy Storage Materials*, 2021, 43, pp.337-347. 10.1016/j.ensm.2021.09.015 . hal-03610978

HAL Id: hal-03610978

<https://u-picardie.hal.science/hal-03610978>

Submitted on 16 Oct 2023

HAL is a multi-disciplinary open access archive for the deposit and dissemination of scientific research documents, whether they are published or not. The documents may come from teaching and research institutions in France or abroad, or from public or private research centers.

L'archive ouverte pluridisciplinaire **HAL**, est destinée au dépôt et à la diffusion de documents scientifiques de niveau recherche, publiés ou non, émanant des établissements d'enseignement et de recherche français ou étrangers, des laboratoires publics ou privés.



Distributed under a Creative Commons Attribution - NonCommercial 4.0 International License

Carbon-Binder Migration: A Three-Dimensional Evaporation Model for Lithium Ion Batteries

*Teo Lombardo,^{1,2} Alain C. Ngandjong,^{1,2} Amal Belhcen^{1,2} and Alejandro A. Franco^{1, 2, 3, 4, *}*

¹ Laboratoire de Réactivité et Chimie des Solides (LRCS), UMR CNRS 7314, Université de Picardie Jules Verne, Hub de l'Energie, 15, rue Baudelocque, 80039 Amiens Cedex, France

² Réseau sur le Stockage Electrochimique de l'Energie (RS2E), FR CNRS 3459, Hub de l'Energie, 15, rue Baudelocque, 80039 Amiens Cedex, France

³ ALISTORE-European Research Institute, FR CNRS 3104, Hub de l'Energie, 15, rue Baudelocque, 80039 Amiens Cedex, France

⁴ Institut Universitaire de France, 103 Boulevard Saint Michel, 75005 Paris, France

* corresponding author: alejandro.franco@u-picardie.fr

ABSTRACT

Li-ion battery electrode manufacturing is raising broad interest from both experimental and computational perspectives, due to its impact on the electrode and cell cost, mechanical and electrochemical properties. Among the different manufacturing processes, drying can trigger heterogeneities within the electrode mesostructure because of additive migration. Despite acknowledging that these heterogeneities significantly affect electrode properties, the drying step is often under evaluated at the experimental level and modelled through homogenized approaches. In this work, we present the first physics-based three-dimensional model able to mimic additive migration during drying, unlocking the generation of three-dimensional heterogeneous electrode mesostructures. We analyzed the effect of drying rate on the final electrode mesostructure, the dynamics of additive migration and how the developed heterogeneities affect the following manufacturing step, *i.e.* calendaring. The results are in agreement with previous experimental findings and indicate trends not previously disclosed. Lastly, the implementation of complex drying protocols (three-stage drying) was tested and compared to its experimental counterpart.

KEYWORDS

Lithium-ion battery, drying, carbon-binder domain, electrode mesostructure, manufacturing

1. INTRODUCTION

Li-ion battery (LIB) is being recognized as one of the key technologies of our time.¹⁻³ LIBs can potentially unlock the commercial success of electric vehicles (EVs)⁴⁻⁶ and lead to more flexible electric grids.⁷ Nonetheless, high electrochemical performance and cycle life, low cost and CO₂ footprint, and a stable raw materials supply chain are essential pre-requisites to make sustainable LIB production upscale.⁸⁻¹⁰ In this context, international actions underlining the importance of sustainable LIB production, as the European¹¹ and global¹² battery alliance and the battery passport,¹³ are particularly important. One way of improving LIB performance and decreasing their cost is through novel materials. However, after three decades of commercial success of LIBs, the cathode and anode chemistries are still similar to the ones commercialized in 1991 by Sony (LiCoO₂ | graphite), namely layered transition metal oxides (as LiNi_xMn_yCo_zO₂) cathodes and carbon-based anodes, respectively.¹ An alternative path to enhance LIB performance, cost and CO₂ footprint relies on optimizing electrode, cell and battery pack manufacturing.¹⁴⁻¹⁸ Electrode production alone accounts for ~40% of the overall production cost and, in between the different manufacturing processes, >50% comes from slurry coating and solvent evaporation.¹⁹ Even though the exact impact of coating and drying in LIB cost varies as a function of the industrial facilities, manufacturing protocols and materials used,²⁰⁻²² these steps are the most expensive ones in terms of electrode manufacturing.²⁰

Studying experimentally the drying process for high solid content (SC) dispersions, as LIB slurries, requires specific equipment, which often need to be built *in house*, and sophisticated strategies. The group of Professor Schabel²³⁻²⁶ published a series of experimental works aiming to investigate drying for graphite-based slurries. In these studies, they demonstrated that: (i) high drying rate (HDR) leads to a gradient in binder distribution along the electrode thickness,

lowering electrode adhesion to the current collector. A strong binder-carbon affinity was also observed, suggesting that HDR could lead to a gradient in terms of carbon distribution as well; (ii) additive migration is not a linear process, it exists a specific time range in which it occurs; (iii) slurry drying is composed of two drying regimes, first the slurry film shrinks until reaching the final electrode thickness and then the pores start emptying until complete solvent evaporation. Both (ii) and (iii) were extensively demonstrated by them and other groups by using adhesive measurements,²³ a devoted experimental set-up to follow solvent evaporation through fluorescent measurements²⁴ and three-stage drying protocol,²⁶ upon others.^{27,28} **In addition, it should be underlined that these findings are not only useful for better understanding additive migration, but they can be used as a highly trustable reference for setting new models aiming to reproduce the trends previously identified and suggest new ones, as it was done in the work presented here.**

On the one side, binder migration is widely accepted among the battery community and it was observed through energy dispersive X-ray,²⁸⁻³⁰ Raman³¹ and Real-time fluorescent spectroscopy.³² On the other side, the observation of conductive additive migration is hampered by the presence of carbon in both binder and conductive phases, but it is supported by experimental observations for both LIB cathodes and anodes.^{23,28} The main reason of migration seems to be convective and capillary forces developed during drying, while diffusion tend to re-homogenize the system.²³ Fast drying and additive migration is typically detrimental for electrochemical performance and cycle life,³³⁻³⁵ promoting electrode cracking (particularly severe for the case of thick electrodes and water processing),^{36,37} poorly interconnected and heterogeneous electrode mesostructures,^{28,29} and poor adhesion to the current collector.^{23,34}

From a computational perspective, the physical complexity of solvent evaporation in high SC suspensions makes challenging the development of devoted physics-based models. Most of the approaches used today relies on 1-dimensional (1D) continuum models^{27,38} or 2-dimensional (2D) discrete ones.^{28,39} However, it was previously demonstrated by us⁴⁰⁻⁴⁵ and others⁴⁶⁻⁴⁹ the advantages of using 3-dimensional (3D) models rather than 1D or 2D ones, especially when considering the carbon-binder domain (CBD) phase together with the active material (AM) one.. In general, the main reason behind the interest for 3D electrode mesostructures is the acknowledgement of the strong link between 3D mesostructure and electrode properties, which has been demonstrated from both experimental and computational perspectives.^{29,42,43,50-53} In particular, 3D physics-based modeling allows generating 3D electrode mesostructures in a more reliable way compared to stochastic approaches^{54,55} and without the need of expensive and not routinely employable instruments, as for instance synchrotrons, required for X-ray tomography techniques.^{56,57}

To date, only three modeling approaches, considering both AM and CBD particles, were published for 3D LIB slurry drying: the one reported by Srivastava *et al.*⁴⁶, the one reported by us^{40,42,43,45} and Forouzan *et al.*⁵⁸ and the one reported by us⁵⁹ and Nikpour *et al.*⁶⁰ All these approaches have been developed through the open-source molecular dynamics software LAMMPS.⁶¹ Srivastava *et al.* considered the solvent implicitly by applying a mean-field viscous drag to particle motion, while the evaporation was performed simply by shrinking the slurry structure until reaching the desired electrode thickness. Our 3D manufacturing computational workflow⁴⁰ accounts for the solvent at the slurry phase by expanding the CBD particles and decreasing their density. This makes the CBD at the slurry phase an effective particle enabling to account for carbon, binder and solvent, as extensively discussed by us in a previous work.⁴¹ The

drying is performed by shrinking the CBD diameter to remove the solvent, leading to particle rearrangement and to the dried electrode mesostructure. An advantage of this approach, compared to the one of Srivastava *et al.*, is that the macroscopic electrode features (porosity, density, thickness) arise from particle interactions, rather than being imposed by shrinking the simulation box. This allows comparing these macroscopic observables with their experimental counterpart in order to parametrize the model, as previously reported.^{40,58} Lastly, a recent evolution of this second approach was reported by us⁵⁹ and Nikpour *et al.*⁶⁰, whose principal characteristic is separating the carbon, binder and nanopores, considered into the CBD particles, and the solvent, accounted through devoted solvent “particles”. However, none of the approaches discussed above can output strongly heterogeneous electrode mesostructures, as the ones obtainable experimentally through fast drying^{28–31}, which is the main reason behind the development of the model presented in this article.

The goal of this work is to propose a first physics-based 3D simulation workflow able to model CBD migration during drying. First, the model is presented and discussed in detail. Then, the impact of evaporation rate on the simulated electrode mesostructure is discussed in terms of its structural features, with a particular interest on the phases (AM, CBD, pores) distribution along the electrode thickness. Afterwards, we analyze how calendaring affects the heterogeneities developed during drying and we assess the model capability of simulating complex drying protocols (three-stage drying). Lastly, an overview on the results obtained and the model perspectives and availability to a broad public are presented.

2. MODEL WORKFLOW

This section discusses the critical aspects of our modeling approach, and in particular.: (i) the slurry phase, (ii) the strategy used to model solvent removal and CBD migration, (iii) particles sedimentation, (iv) the consideration of the two drying regimes and (v) the FFs utilized. A schematic overview of the model workflow is illustrated in Figure 1.

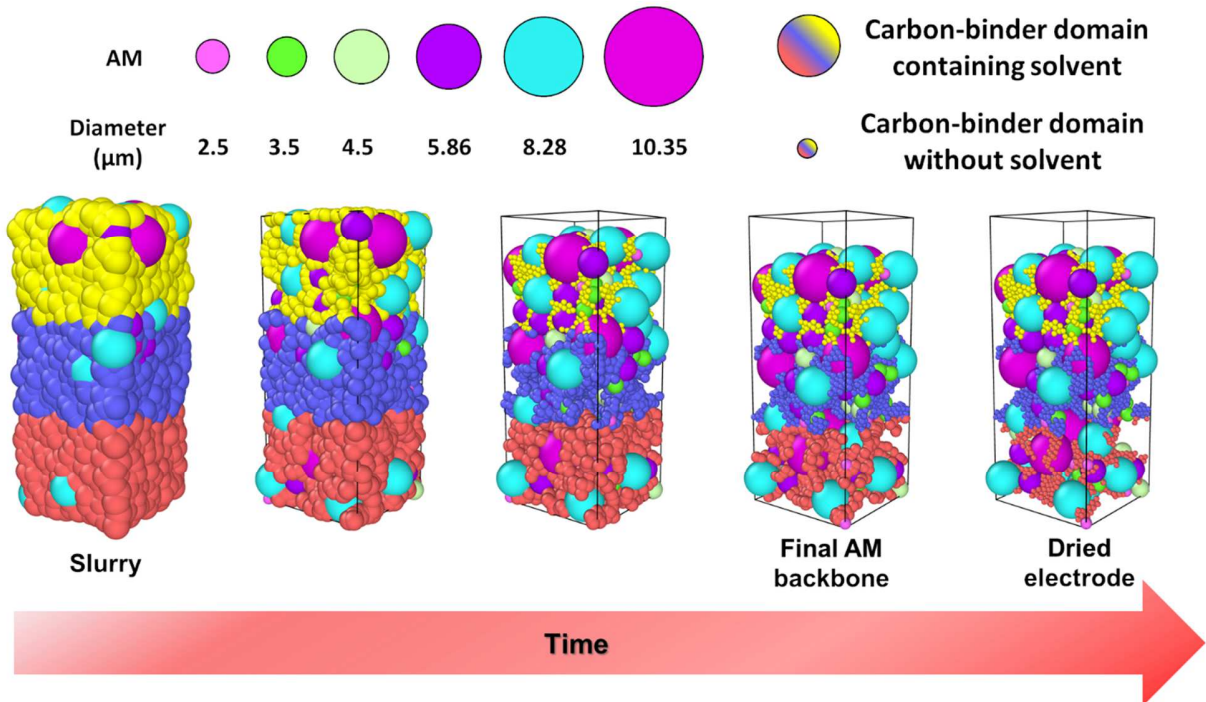


Figure 1. Schematic representation of the 3D drying model developed in this work. The AM sizes come from the experimental AM ($\text{LiNi}_{0.33}\text{Mn}_{0.33}\text{Co}_{0.33}\text{O}_2$) particle size distribution considered⁴¹, while the CBD size can be tuned by the operator and depends on the time undergone from the beginning of the evaporation and on the drying rate utilized. In this work, the initial CBD diameter (before drying) was 5.7 μm, while its final diameter (end of drying) was 1.3 μm, accounting for carbon, binder and nanopores. The three colors associated to the CBD phase link to the three regions (bottom, middle and top) defined for the computational workflow utilized to simulate drying.

The slurry phase is validated by comparing the experimental and simulated slurry shear-viscosity curves, as previously discussed by us in full details in Reference ⁴¹ and as briefly reported in section S1 of the supplementary information. The AM particle size distribution arises from devoted *in house* experimental measurements, while the CBDs are effective particles accounting for carbon, binder and solvent. Both AM and CBD particles are considered to be spherical. From one side, this limits this approach to approximately spherical AM particles, as for instance certain commercial $\text{LiNi}_{0.33}\text{Mn}_{0.33}\text{Co}_{0.33}\text{O}_2$ (NMC). From the other side, this requires post-processing processes (as meshing⁶² or expand-erode approaches^{59,63}) to made the CBD phase more realistically looking before assessing, for instance, the associated electrochemical performance. Computational workflows able to consider non-spherical particles and employable in the context of the drying model presented in this article are currently being developed in our research group and will be the subject of a future publication. Briefly, this kind of approach can rely either on ellipsoidal particles or on rigid bodies, meaning agglomeration of spherical particles connected in such a way to form non-spherical shapes and treated as a single particle. Concerning the case study reported here, the slurry was composed of NMC, Carbon black (C65), polyvinylidene difluoride (PVdF) and N-Methyl-2-pyrrolidone (NMP). The weight ratio considered is 94:3:3 (NMC:C65:PVdF), with a SC of 65%. The SC is defined here as the mass of the solid components (NMC+C65+PVdF) divided by the total mass of the slurry (solid components + solvent). All the results presented in this article were obtained by using as starting point the same slurry geometry in order to make the different results directly comparable. This geometry is obtained by first generating a random structure, requiring seed numbers, and then running a physics-based simulation, as extensively discussed in Ref. ⁴¹. The FF parameter values adopted for the slurry simulation are reported in Table S1 of the supplementary information. The

choice of the initial seed numbers have a small impact of the final slurry geometry, as we have previously reported.⁶⁴ Therefore, the role of the initial slurry geometry was verified through the utilization of different seed numbers, for which similar results compared to the ones reported in the main text have been obtained (section S3 of the supplementary information).

As briefly presented in the introduction and extensively discussed in our previous works,^{40,45,64} drying is modelled by shrinking the CBD particles and increasing their density. Keeping in mind that evaporation is a surface phenomenon, it affects first the top of the slurry, while its bottom is initially less affected. The key idea of the approach proposed in this article is to modulate the speed of solvent removal as a function of the CBD particle position. In particular, CBD particles at the top of the slurry shrink faster than the ones in the bottom. In this work, as illustrated in Figures 1 and 2A, the CBD particles are classified in three groups as a function of their z-coordinate (slurry thickness): the ones in the first third (bottom, referred as CBD1), the ones in the second third (center, referred as CBD2) and the ones in the last third (top, referred as CBD3). Then, we defined the shrinking speed of CBD1 (v_{bottom}) as the speed needed to remove all the solvent at the end of the simulation. In other terms, and considering that CBD1 particles are the ones with the slower shrinking speed, this means assuming that the solvent removal is complete at the end of the drying. Afterwards, a relative shrinking factor (RSF) is defined as v/v_{bottom} for the center and top CBDs, where v is the shrinking speed for CBD2 and CBD3, respectively. Taking in mind that evaporation occurs faster in the top of the slurry with respect to its bottom, both the RSFs are >1 . The higher these RSFs, the faster the solvent removal, *i.e.* the higher the drying rate. For more details on how the RSFs are implemented, the interested readers are referred to section S2 of the supplementary information. **Faster shrinking speeds of the CBD particles result in more free space in the associated slurry region, leading to a higher particle degree of**

freedom. However, this aspect alone would not be enough to account for the convective and capillary forces causing additive migration experimentally. For this, it should be considered that the attractive interactions of the CBD particles, controlled through the force fields (FFs) utilized (presented below), increases when the solvent is removed. This was found to be needed, in all the previous versions of this model, to obtain electrodes with approximately the same porosity, density and mechanical properties of their experimental counterpart.^{40,45,58,64} In the context of a model in which the solvent is removed asymmetrically, this leads to higher attractive forces of the CBD phase in the top and middle regions compared to the bottom one. These stronger attractive interactions and the higher amount of space available, both dictated by the asymmetric CBD shrinking speeds adopted, translate in a force gradient towards the top of the slurry that affects the dynamics of lighter particles, here CBD. This mimics the role of convective and capillary forces and leads to results that, to the best of our knowledge, agree with all the experimental findings reported so far, as it will be shown in the next sections.

Another important aspect that need to be considered is particles sedimentation, which is leaded by gravity and atmospheric pressure. Gravity has been accounted by considering an extra acceleration term (equal to the gravitational acceleration) on each particle. Concerning the atmospheric pressure, LAMMPS allows applying a barostats⁶⁵ (*i.e.* controlling the pressure applied to the simulated system) only if all the boundary conditions are considered as periodic. Along this work, we considered x and y boundary conditions as periodic, while z is considered as not periodic to model consistently the drying and associated additive migration. Therefore, the following computational strategy was used to account for atmospheric pressure: (*i*) the force acting on the whole slurry due to the atmosphere (F_{atm}) was calculated as the atmospheric pressure ($P_{atm} = 101325$ Pa) by the slurry surface (S_{slurry}) and (*ii*) a fraction of F_{atm} was added

to each particle as a function of its surface area (S_i) normalized to the sum of surface areas of all the particles in the system. Considering all the above, sedimentation along the simulation is mainly driven by bigger and heavier AM particles, as expected experimentally.^{23,28} Another possible approach would be the application of gravity only, which should be enough if simulating explicitly the drying time, typically in the order of minutes at the industrial scale and hours at the lab scale. However, this would be prohibitively expensive, as recently highlighted in a similar context.⁶⁰ In this context, a third possible approach is using an effective gravity, higher than the actual one, to account for this difference in time scales.

As discussed in the introduction, solvent evaporation is composed of two drying regimes: first the slurry shrinks until its final thickness, defining the final AM backbone, and then the pores start emptying.²⁵ In the computational approach developed here, the final AM backbone was defined by freezing the AM particles when reaching a desired bulk porosity (~46%) for all the evaporation rates considered. **It should be stated, however, that the porosity of electrodes dried at different drying rates could differ, but to the best of our knowledge no clear trends have been previously disclosed, neither experimentally nor computationally. Nonetheless, the same trends in terms of CBD migration during drying were found even when not imposing a final electrode porosity, as shown in section S5 of the supplementary information. In the following, we will focus on the approach approximating** the same macro features (porosity, density, loading) for electrodes dried at different DRs, which enables focusing on the only effect of DR on CBD migration and its impact on the electrode characteristics. Furthermore, it should be underlined that an aspect of our computational workflow is the implicit consideration of a (solid) CBD nanoporosity of ~50% , , as found experimentally⁶⁶ and as we discussed previously⁴⁰. In this

manuscript, we will refer to “bulk” porosity when considering the pore phase only and to “overall” porosity when accounting for the bulk pores plus the CBD nanoporosity.

Lastly, the FFs used for the drying simulation are the same of the slurry one, namely Lennard-Jones (LJ), accounting for adhesive forces between particles, and granular Hertzian (GH), accounting for the mechanical properties of the system, as extensively discussed by us in previous studies.^{40,41,45,64} However, the FF parameter values change during drying, going from the ones of the slurry (mimicking a liquid-like system) to the ones of the electrode (mimicking a solid system) through two linear regimes. **Briefly, the main difference between slurry and electrode FF parameter values, explicitly reported in Table S1 of the supplementary information, is an increase of attractive interactions and elastic properties, accounting for stronger particles links due to binder bridges and greater stiffness, respectively.** The two linear regimes link to the two drying regimes observed experimentally and discussed in the introduction, and the transition from the first to the second one occurs at the same time in which the final AM particles backbone is reached.

3. RESULTS AND DISCUSSION

The first and most important feature of the drying model developed is its capability of mimicking additive (here CBD) migration as a function of the DR used. The DR was defined through the RSF applied to CBD2 (central region) and CBD3 (top region), *i.e.* the higher those values, the higher the DR. Figure 2A illustrates the 3D electrode mesostructures obtained at different DRs, with the RSFs of the center (RSF₂) and top (RSF₃) CBD particles at their bottom, reported as RSF₂ / RSF₃. The RSF of the CBD in the bottom (CBD1) is kept constant to one for definition, as discussed in the previous section. From these 3D rendering it can be already noted

that the higher the DR (from left to right) the higher the degree of heterogeneity, *i.e.* more CBD particles in the top region of the electrode with respect to its bottom. To quantify it, the evolution of CBD fraction for each region (CBD1, CBD2 and CBD3) during drying is reported in Figure 2B for the four DRs considered. These results can be summarized as: *(i)* the higher the DR, the higher the fraction of CBD3 at the expense of CBD2 and CBD1. *(ii)* CBD migration does not take place during the whole drying step, but rather in a specific time range. *(iii)* the times at which CBD migration starts and ends depend on the DR, and particularly CBD migration starts and ends before for higher DRs compared to lower DRs. Both *(i)* and *(ii)* were found experimentally, as discussed in the Introduction and as shown in Figure 2C, indicating that the model is capable of reproducing these trends. To the best of our knowledge, *(iii)* was not previously reported, calling for further experimental studies aiming to verify and eventually quantify this phenomenon.

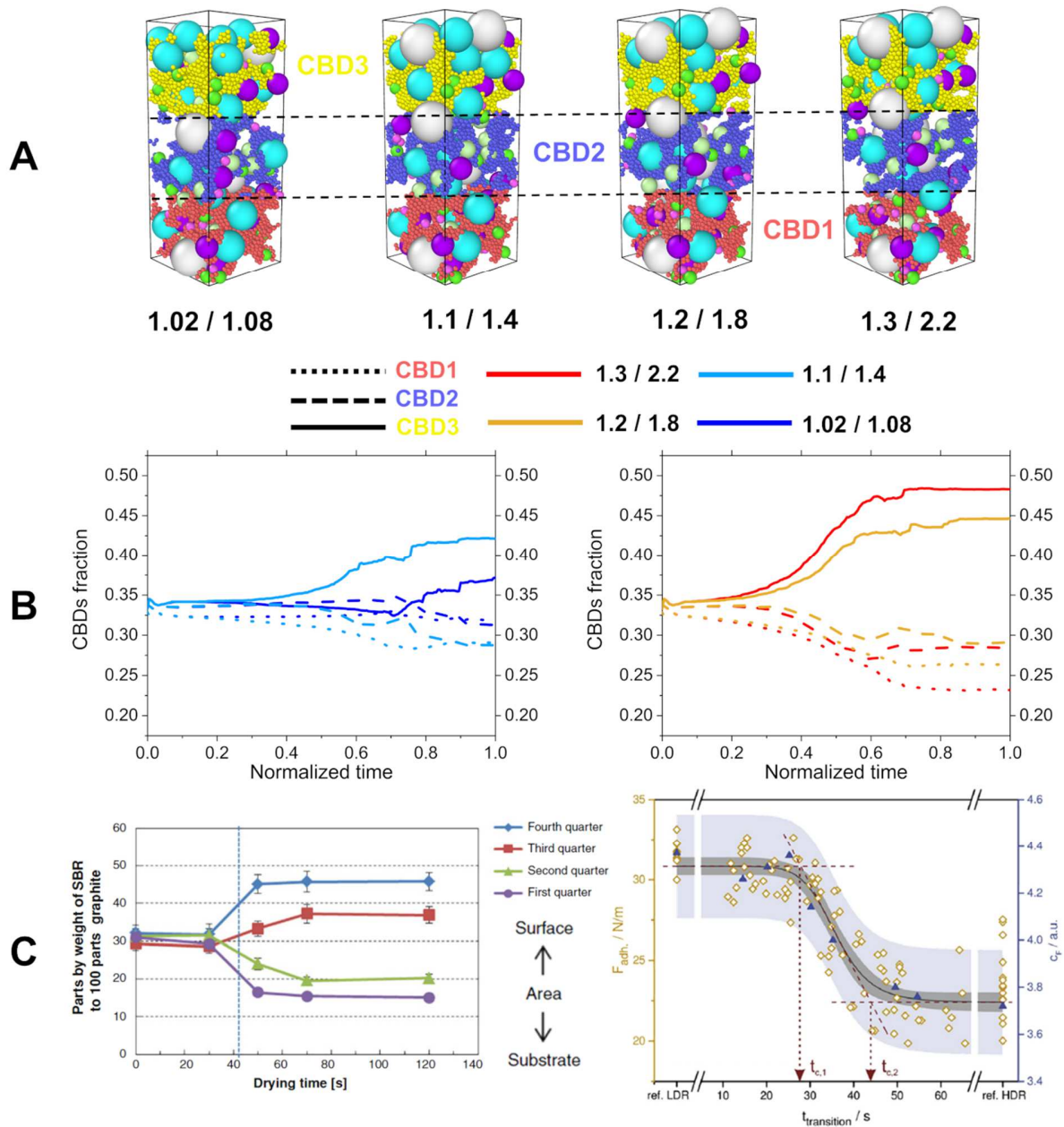


Figure 2. A) 3D rendering of four electrode mesostructures obtained from the same slurry but changing the drying conditions. The RSFs of CBD2 / CBD3 for each case is reported below the associated structure. The drying rate increases from left to right. The four electrodes have the same surface area ($26.7 \times 26.7 \mu\text{m}^2$), an active loading of 13.6 mg cm^{-2} , a density of 2.24 ± 0.01 and a bulk/overall porosity of $0.458 \pm 0.004 / 0.518 \pm 0.004$. The errors reported here are the standard deviations, while bulk/overall porosity stand for the volume fraction of the bulk pore only and the bulk pore plus the nanoporosity in the CBD phase (50%), respectively. B) Evolution of the fractions of CBD1 (dot line), CBD2 (dash line) and CBD3 (full line) during drying. Here, cold colors indicate low/middle drying rates, while hot colors indicate middle/high drying rates. A normalized time of 0 indicates the slurry phase, while at 1 the drying is complete. C) Previous

experimental observations of binder migrations occurring during drying through Raman spectroscopy (left) and adhesive measurements (right). (left) Figure adapted from Reference ³¹. Copyright 2013 Springer. (right) Figure adapted from Reference ²³. Copyright 2016 Elsevier.

To further characterize the electrode mesostructure, the volume fractions (AM, CBD and macro pores) evolution as a function of the electrode thickness is reported in Figure 3. In terms of solid phases (Figure 3A), it can be noted that the electrodes dried at lower DRs contain more AM and CBD in the first half of their thickness and less in the second half, when compared to the ones dried at higher DRs. Concerning the CBD phase, no significant differences can be observed for the central region of the electrodes. If this trend was expected and already discussed for the CBD phase (Figure 2B), the AM distribution is linked to particle sedimentation, and particularly to the minor time available for sedimentation during fast drying. In our model, it was found that the porosity defined as set point to switch from the first regime to the second one, where the final AM backbone is formed, was reached at normalized times of ~ 0.79 and ~ 0.62 for the lowest and highest DRs, respectively. The middle DRs (1.1 / 1.4 and 1.2 / 1.8) show intermediate transition times between these two. This means that the AM particles had $\sim 27\%$ more time to sediment when dried at the lowest DR with respect to the highest one, leading to higher concentration of this phase in the bottom of the electrode. The pore phase (Figure 3B) follows approximately the reverse trend when compared to the AM volume fraction, indicating that the electrode bulk porosity is mainly controlled by the biggest particle location.

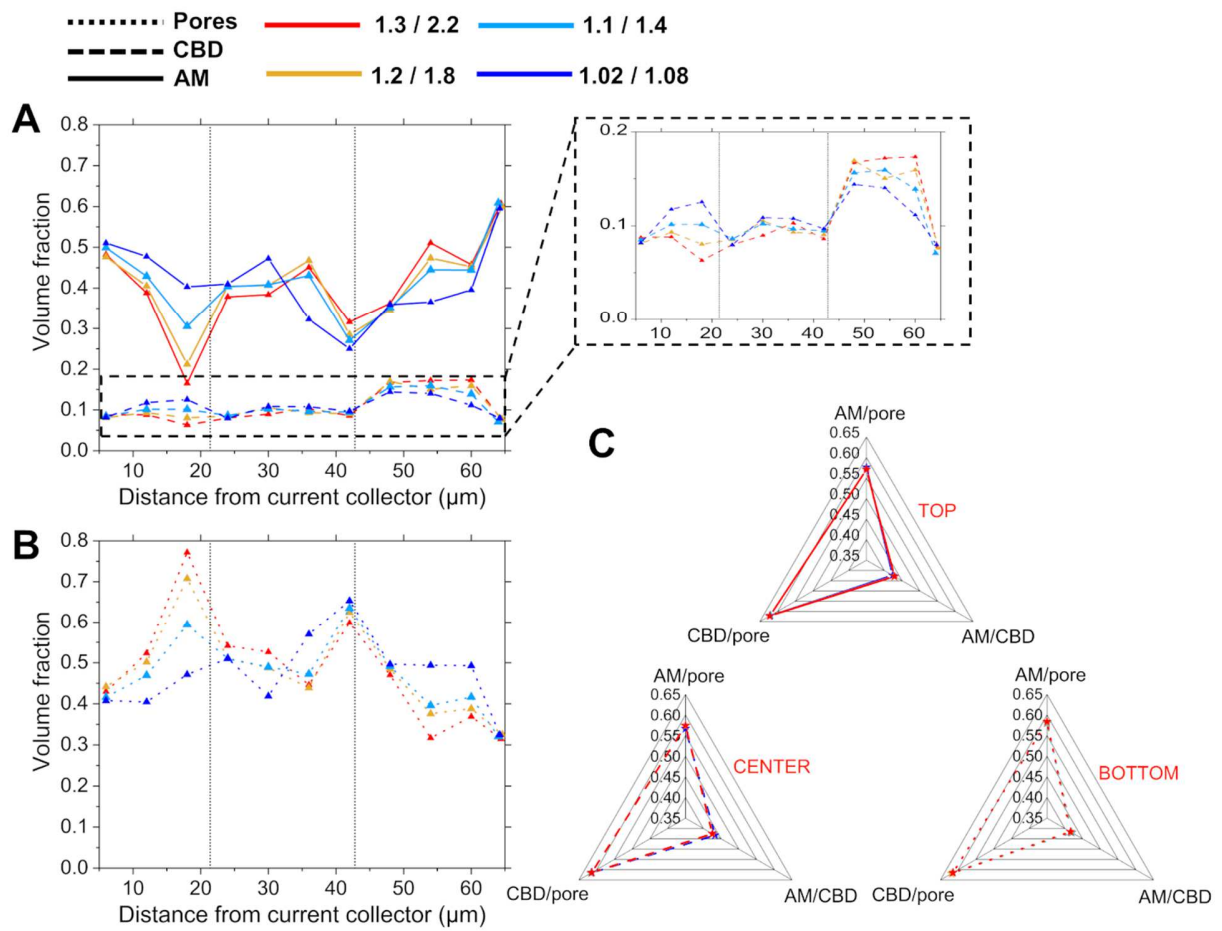


Figure 3. A) Evolution of AM, CBD and B) bulk pores volume fractions as a function of the electrode thickness for electrodes dried at different DRs (legend on the top left). The vertical dot lines separate the three electrode regions defining the three RSFs during drying (Figure 2A). C) Percentage of AM surface in contact with pore (AM/pore) or CBD (AM/CBD) phases and percentage of CBD surface in contact with the pore phase (CBD/pore) for the same electrode regions (top, center and bottom) of A and B. Here the top, center and bottom regions are indicated with full, dash and dot lines, respectively.

Besides the distribution of AM, CBD and pore volume fractions, interfaces between the different phases is a key characteristic as well. Figure 3C shows that the approach employed in this work

was capable of keeping substantially constant the percentage of AM surface in contact with both CBD and pore and the percentage of CBD surface in contact with the pore phase. This indicates that the application of different DRs, through the computational workflow proposed here, affects specifically the phase distributions (Figure 2 and 3A and B), while the interfaces are rather controlled by the FF parameter values utilized, here kept constant (Table S1).

One could wonder if the heterogeneities developed during drying are kept along the next manufacturing steps or not, and in the first case to which degree. To study this aspect, the four electrode mesostructures discussed above were compressed, mimicking the calendaring step, by reducing their thickness of 25% and reaching a bulk and overall porosities of 0.243 ± 0.006 and 0.324 ± 0.005 , respectively. Figure 4 shows a schematic of the electrode mesostructures evolution during compression (A) and the volume fractions of the calendared electrodes along their thickness (B).

Figure 4B underlines two main aspects: *i*) compression reduces the volume fraction of the pore phase asymmetrically, *i.e.* higher particle compaction, and then lower porosity, is observed in the top side of the electrode compared to its bottom; *ii*) the differences between the electrode mesostructures are less pronounced after calendaring with respect to the just dried electrodes (Figure 3), but some differences are still observable. *i*) is understandable considering that the compression is performed by applying a plane on the electrode top side, which is moved down to mimic the calendaring rolls;^{40,67} then, the first particles being compacted are the ones in the electrode top layer. However, it should be mentioned that an aspect missing in the computational workflow used here is the role of rolls' temperature, which is known to induce higher deformability of the binder phase and that could play a role in its reorganization during calendaring.⁶⁸

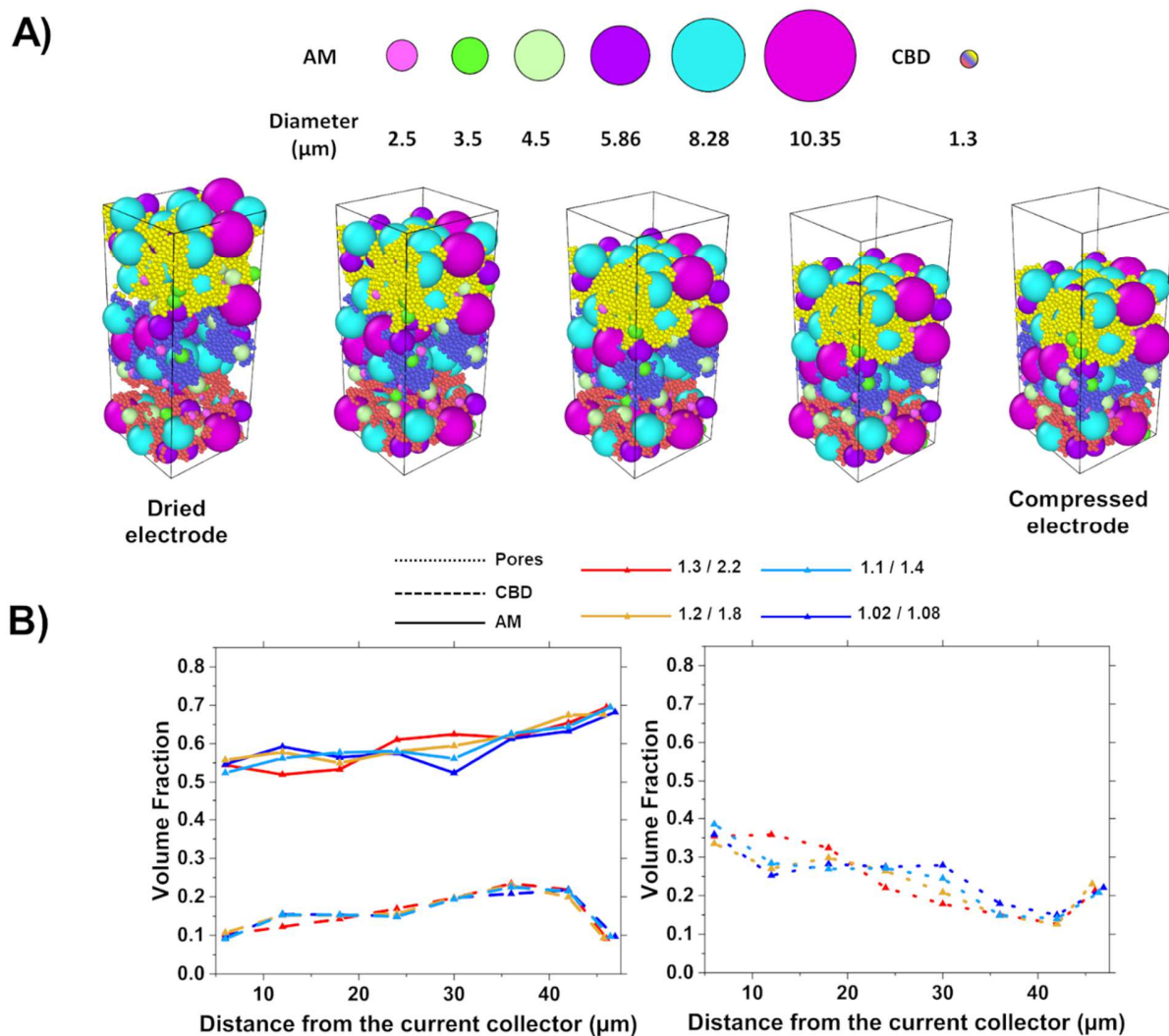


Figure 4. **A)** Evolution of the electrode mesostructures during calendaring for the case of the electrode 1.3 / 2.2. The different colors (red, blue and yellow) of the CBD particles (indicating the 3 regions defined during drying, Figure 2) are kept just as a guideline for the eyes, but here all the CBD particles have the same physical properties. **B)** Evolution of AM and CBD (left) and bulk pores (right) volume fractions as a function of the electrode thickness.

Concerning point *ii*), to better evaluate the role of compression in leveling, but not completely removing, the dried electrode heterogeneities, a direct comparison between dried and calendered electrodes is depicted in Figure 5. In particular, Figure 5 reports the relative phase difference (RPD) for both compressed and just dried electrodes along their thickness. The RPD is defined as the ratio between the volume fraction of a (un)compressed electrode and the volume fraction of the (un)compressed one initially dried at the lowest DR tested (1.02 / 1.08). Therefore, the RPD offers a quantification of how different is the analyzed electrode mesostructure compared to the less heterogeneous one, and particularly the closer the RPD to 1, the lower the differences. Furthermore, to easily compare compressed and just dried electrodes, their associated RPD is reported as a function of their normalized thickness (0% stands for current collector side, 100% for separator side). From this analysis, it is possible to note that the RPDs of the calendered electrodes (dash lines) are systematically lower compared to the non-calendered ones (full lines), underlining that the compression helps in leveling the heterogeneities arising from fast drying. Lastly, comparing the RPDs of AM, CBD and pore phases for the different electrodes considered, left to right in Figure 5, underlines that the electrode mesostructures have a memory, meaning that the structure arising from one manufacturing step affects the following one. In the case study reported here, this reads as different calendered electrode mesostructures when applying the same calendering protocol, but applied to electrodes dried differently.

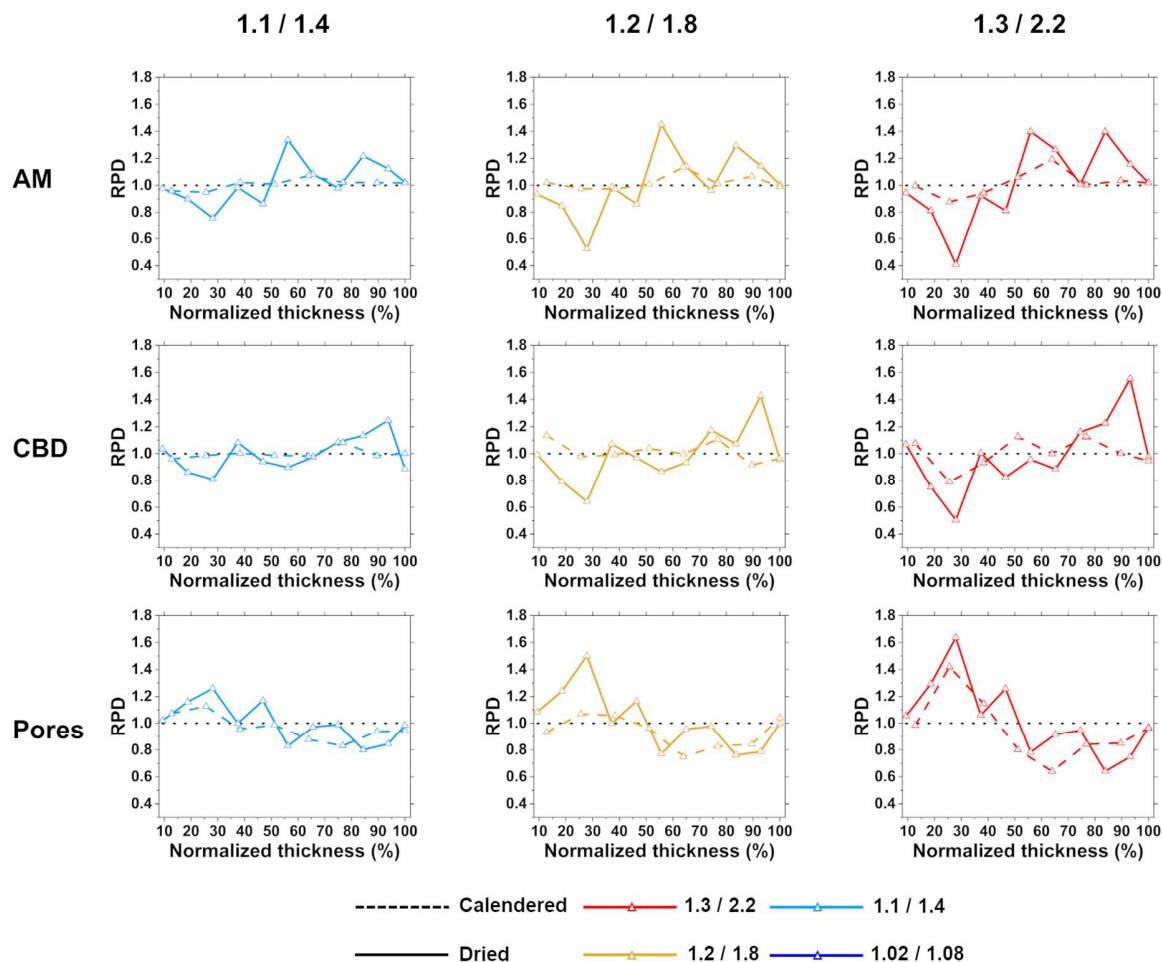


Figure 5. Evolution of the relative phase difference (RPD) for AM, CBD and (bulk) pore phases along their normalized thickness (0% stands for current collector side, 100% for separator side) for electrodes compressed (Calendered) or not (Dried) that were dried at different DRs. The black dotted line is a guideline for the eyes indicating an RPD equal to 1.

4. THREE-STAGE DRYING

Another aspect of the model that was tested is its capability of reproducing complex drying protocols. In particular, here we focused on the three-stage drying protocol proposed and developed by Jaiser *et al.*,²⁶ in which they applied an high DR at the beginning and at the end of

the drying, while a low DR in between. Taking advantage of additive migration occurring during the low DR period, this strategy allowed obtaining electrodes with the same properties of the ones fully dried at low DR and reducing the overall drying time (and then the electrode costs). In the following, we have applied the same logic for three different scenarios, *i.e.* setting a very low drying rate (1.02 / 1.03) at the beginning, mid or end of the drying protocol, while a high DR (1.2 / 1.8) for the rest, as illustrated in Figure 6 A. Figure 6 B shows that applying low DR at both the beginning and middle of the drying is beneficial in decreasing CBD migration, being the second case the best condition, similarly to the scenario tested by Jaiser *et al.* On the contrary, applying low DR at the end of the drying is not effective in terms of reducing CBD migration, which is understandable considering that, at that stage in which LD rate is applied in such a scenario, the majority of migration already occurred (Figure 2). This shows that the model can capture qualitatively the trend discussed by Jaiser *et al.*, but the quantitative results differ. Indeed, on the one hand they found that applying low DR rate in the middle of the drying allowed reaching the same structural properties, using adhesion with the current collector as metrics, of the electrode fully dried at low DR rate. On the other hand, in our case this three-stage dried electrode is still more heterogeneous with respect to the one dried at 1.02 / 1.08 (figure 6 C), despite the use of a particularly low DR (1.02 / 1.03) in the three-stage scenario, indicating that there is still room for improvements of the model.

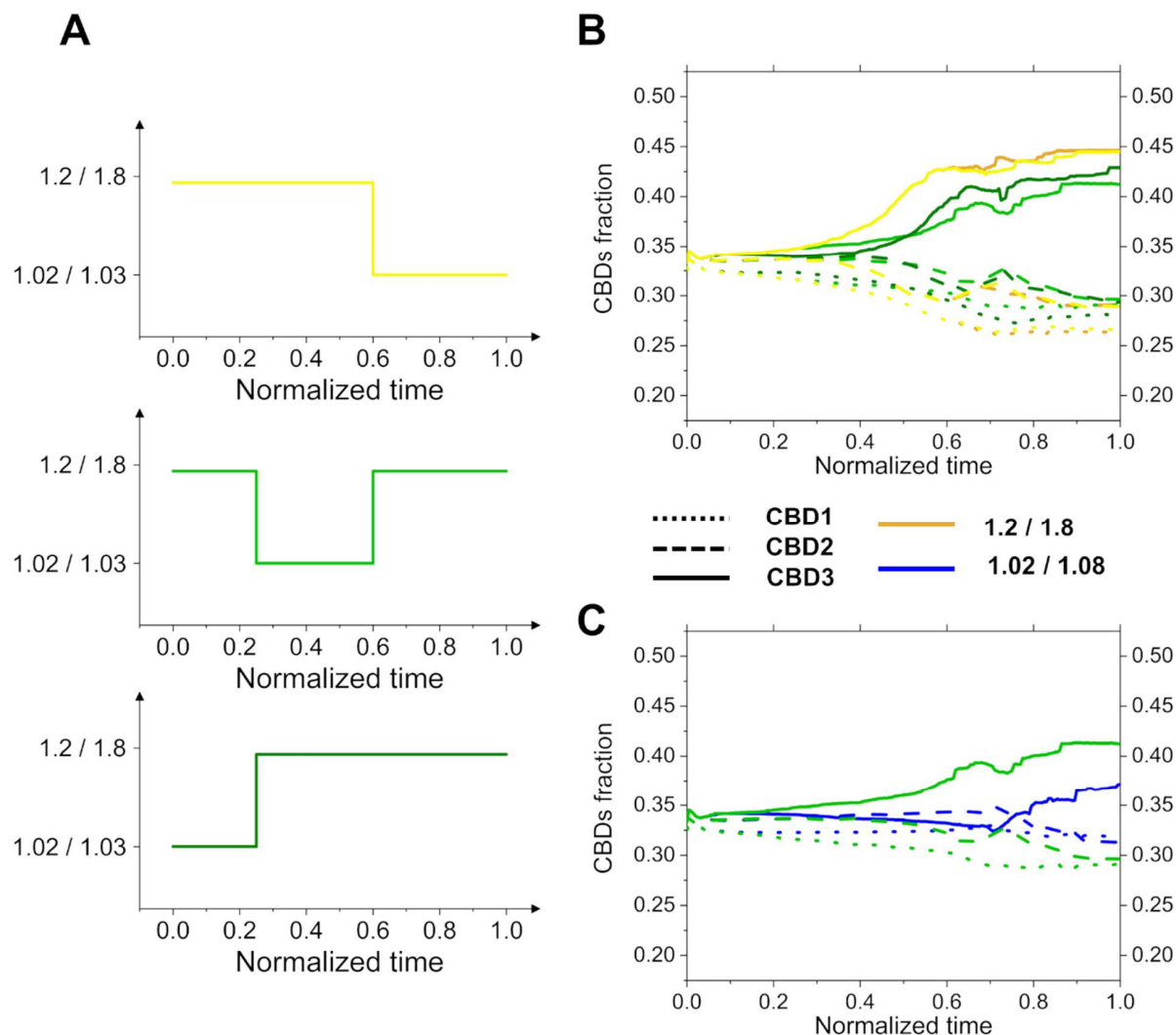


Figure 6. **A)** Schematic of the three-stage drying protocols implemented in this work, where the low DR rate step was applied at the end (yellow), middle (light green) and beginning (dark green) of the drying protocol. **B)** Comparison between the electrode fully dried at 1.2 / 1.8 and the ones dried with the three-stage drying protocols defined in A. **C)** Comparison of the less heterogeneous three-stage dried electrode and the one fully dried at 1.02 / 1.08.

5. CONCLUSIONS

In this work, we presented the first 3D physics-based model able to simulate drying by explicitly considering additive migration, which was applied to the case of NMC-based slurries and electrodes. The key idea that allowed to reach such a result is to modulate the speed of transition from a liquid-like system (the slurry) to a solid one (the electrode) as a function of the slurry thickness (here divided into 3 regions), *i.e.* faster at the top with respect to its bottom. The DR was defined as a function of the speed of this transition in the top and middle regions compared to the bottom one. Four different DRs were tested, outputting four different electrode mesostructures that were analyzed in terms of their structural characteristics. In particular, the results underlined that: *(i)* the higher the DR, the higher the fraction of CBD3 (top region) at the expense of CBD2 (middle region) and CBD1 (bottom region). *(ii)* CBD migration does not take place during the whole drying step, but rather in a specific time range. *(iii)* the time at which CBD migration starts and ends depends on the DR. *(i)* and *(ii)* agree with the experimental findings reported so far, while *(iii)* was not disclosed yet, calling for further studies in this direction. Then, the electrodes dried at different DRs were compressed of 25 % with respect to their initial thickness, mimicking calendaring. It was observed that this step induces a gradient in the bulk pore volume fraction, lower in its top compared to its bottom, and that allows levelling, but not completely removing, the electrode heterogeneities developed during fast drying. The first observation links to the uniaxial compression applied from the electrode top layer mimicking the calendaring rolls, while the second one highlights that manufacturing processes are interconnected and that the final electrode properties arise from an interplay between them.

One last model feature that was tested is its capability of reproducing three-stage drying protocols, which were found to be beneficial for reducing manufacturing costs while keeping optimal electrode properties. The results obtained show that our model is able to capture qualitatively such a behavior, confirming that applying high DR at the beginning and end of drying and low DR in between outputs less heterogeneous electrodes.

In terms of perspectives, the computational workflow described in this article should be tested for a wide range of electrode formulation, AM particle size distribution, CBD size and DR to verify its generalizability to different scenarios compared to the one considered here. In that sense, the code developed during this work will be released freely on the ARTISTIC project Github⁶⁹ for any computational researcher possibly interested into it, while it is already implemented in the ARTISTIC computational platform through an user-friendly interface.⁷⁰ This platform is open to the public (freely) and allows experimentalists and not expert researchers to generate electrode mesostructures through the workflow discussed in this work, being free to select the desired electrode composition (weight ratio between AM and CBD), SC, AM particle size distribution, CBD size, drying and calendering conditions, which we hope will lead to a deeper testing of the model in a collaborative way. Lastly, we hope that this work can trigger the development of new 3D computational approaches focused on drying or, more generally, 3D physics-based models able to output heterogeneous electrodes mesostructures, inspiring practical innovations in the energy storage field.

Computational section

The slurry and dried electrode simulations (155 AM and 5821 CBD particles) were performed through the open source molecular dynamics software LAMMPS and took ~6 hours and ~6.5 days by using one and two node(s) (128 GB of RAM) composed of 2 processors (Intel® Xeon® CPU E5-2680 v4 @ 2.40GHz, 14 cores) on the MatriCs platform (Université de Picardie-Jules Verne), respectively. The initial structure (prior the slurry equilibration) was generated to match the experimental composition and AM particles size distribution by locating randomly the AM and CBD particles in a simulation box big enough ($200 \times 200 \times 500 \mu\text{m}$, $x \times y \times z$) to avoid significant particle overlap. All the details about the random structure generation can be found in the Supporting Information of Reference ⁴¹. The slurry simulation was performed in a NPT environment, at 298 K and 1 atm, while the drying simulation was performed in a NVT environment at 353 K and the pressure was considered as described in the model workflow section. The boundary conditions of the slurry simulations were considered as periodic in all the directions (x, y and z). Concerning the drying simulations, two repulsive planes were added at the slurry top and bottom to constrain the z direction, for which not periodic boundary conditions were applied. x and y directions were kept periodic also during the drying. The slurry and drying simulations used a timestep of 1 and 0.1 ns, while the number of timestep was 13×10^6 and 100×10^6 , respectively. The electrode compression was performed by applying a plane to the electrode top (separator side), which was moved down until reducing the electrode thickness of 25% with respect to its not-compressed state. These simulations were performed by keeping the final FF parameter values of the drying simulation (Table S1 in the supplementary information). This simulation was performed in LAMMPS and took approximately 20h by using one node (128 GB of

RAM) composed of 2 processors (Intel® Xeon® CPU E5-2680 v4 @ 2.40GHz, 14 cores) on the MatriCs platform (Université de Picardie-Jules Verne).

The analysis of the volume fractions and interfaces were performed through voxelization of the electrode mesostructures by using a resolution of 0.1 μm .

Conflicts of interest

The authors declare that they have no known competing financial interests or personal relationships that could have influenced the work reported in this paper.

Acknowledgements

The authors acknowledge the European Union's Horizon 2020 research and innovation programme for the funding support through the European Research Council (grant agreement 772873, "ARTISTIC" project). A.A.F. acknowledges Institut Universitaire de France for the support. Results obtained using LAMMPS were achieved thanks to the MatriCS HPC platform from Université de Picardie-Jules Verne, particularly using the ARTISTIC project-dedicated computational nodes. The authors acknowledge Dr. Garima Shukla and Dr. Emiliano N. Primo from LRCS-Amiens (France) for very useful discussions.

Supplementary data

The supplementary Information.pdf file is available free of charge with this article, reporting the slurry phase validation, the FF parameter values used for the slurry, drying and calendaring simulation and some extra details on the computational workflow adopted to apply the different RSFs.

Data and code availability

The code developed along this work will be release freely on the ARTISTIC project Github⁶⁹ in two versions, one accounting for the atmospheric pressure as described in the model workflow section and the second one accounting for it through an effective gravity. In addition, it is already implemented for free in the ARTISTIC computational platform, using here the effective gravity approach, through an user-friendly interface allowing to select the desired electrode composition (weight ratio between AM and CBD), SC, AM particle size distribution, CBD size, drying and calendering conditions.⁷⁰

REFERENCES

- (1) Winter, M.; Barnett, B.; Xu, K. Before Li Ion Batteries. *Chem. Rev.* **2018**, *118* (23), 11433–11456. <https://doi.org/10.1021/acs.chemrev.8b00422>.
- (2) Blomgren, G. E. The Development and Future of Lithium Ion Batteries. *J. Electrochem. Soc.* **2017**, *164* (1), A5019–A5025. <https://doi.org/10.1149/2.0251701jes>.
- (3) Larcher, D. & J.-M. T. Towards Greener and More Sustainable Batteries for Electrical Energy Storage. *Nat. Chem.* **2015**, *7* (January), 19–29. <https://doi.org/10.1038/NCHEM.2085>.
- (4) Opitz, A.; Badami, P.; Shen, L.; Vignarooban, K.; Kannan, A. M. Can Li-Ion Batteries Be the Panacea for Automotive Applications? *Renew. Sustain. Energy Rev.* **2017**, *68*, Part 1, 685–692. <https://doi.org/https://doi.org/10.1016/j.rser.2016.10.019>.
- (5) Ding, Y.; Cano, Z. P.; Yu, A.; Lu, J.; Chen, Z. Automotive Li-Ion Batteries: Current Status and Future Perspectives. *Electrochem. Energy Rev.* **2019**, *2* (1), 1–28. <https://doi.org/10.1007/s41918-018-0022-z>.
- (6) Marinaro, M.; Bresser, D.; Beyer, E.; Faguy, P.; Hosoi, K.; Li, H.; Sakovica, J.; Amine, K.;

- Wohlfahrt-Mehrens, M.; Passerini, S. Bringing Forward the Development of Battery Cells for Automotive Applications: Perspective of R&D Activities in China, Japan, the EU and the USA. *J. Power Sources* **2020**, *459* (March), 228073. <https://doi.org/10.1016/j.jpowsour.2020.228073>.
- (7) Dunn, B.; Kamath, H.; Tarascon, J. M. Electrical Energy Storage for the Grid: A Battery of Choices. *Science* (80-.). **2011**, *334* (6058), 928–935. <https://doi.org/10.1126/science.1212741>.
- (8) IEA (2020), *Global EV Outlook 2020*, IEA, Paris [https://www.Iea.Org/Reports/Global-Ev-Outlook-2020](https://www.iea.org/reports/global-ev-outlook-2020).
- (9) IEA (2021), *Global EV Outlook 2021*, IEA, Paris <https://www.Iea.Org/Reports/Global-Ev-Outlook-2021>.
- (10) IEA (2021), *The Role of Critical Minerals in Clean Energy Transitions*, IEA, Paris <https://www.Iea.Org/Reports/the-Role-of-Critical-Minerals-in-Clean-Energy-Transitions>.
- (11) https://ec.europa.eu/growth/industry/policy/european-battery-alliance_en (Accessed on February 2021).
- (12) <https://www.weforum.org/global-battery-alliance/home> (Accessed on February 2021).
- (13) <https://batterypassport.org/> (Accessed on February 2021).
- (14) Wood, D. L.; Li, J.; Daniel, C. Prospects for Reducing the Processing Cost of Lithium Ion Batteries. *J. Power Sources* **2015**, *275*, 234–242. <https://doi.org/10.1016/j.jpowsour.2014.11.019>.
- (15) Ahmed, S.; Nelson, P. A.; Gallagher, K. G.; Susarla, N.; Dees, D. W. Cost and Energy Demand of Producing Nickel Manganese Cobalt Cathode Material for Lithium Ion Batteries. *J. Power Sources* **2017**, *342*, 733–740. <https://doi.org/10.1016/j.jpowsour.2016.12.069>.
- (16) Turetskyy, A.; Thiede, S.; Thomitzek, M.; von Drachenfels, N.; Pape, T.; Herrmann, C. Toward Data-Driven Applications in Lithium-Ion Battery Cell Manufacturing. *Energy Technol.* **2020**, *8*

- (2), 1–11. <https://doi.org/10.1002/ente.201900136>.
- (17) Günther, T.; Billot, N.; Schuster, J.; Schnell, J.; Spingler, F. B.; Gasteiger, H. A. The Manufacturing of Electrodes: Key Process for the Future Success of Lithium-Ion Batteries. *Adv. Mater. Res.* **2016**, *1140*, 304–311. <https://doi.org/10.4028/www.scientific.net/amr.1140.304>.
- (18) Hawley, W. B.; Li, J. Electrode Manufacturing for Lithium-Ion Batteries—Analysis of Current and next Generation Processing. *J. Energy Storage* **2019**, *25* (July), 100862. <https://doi.org/10.1016/j.est.2019.100862>.
- (19) *Boston Consulting Group Report “The Future of Battery Production for Electric Vehicles”* <https://www.bcg.com/publications/2018/future-battery-production-electric-vehicles> (Accessed on September 2018).
- (20) Schunemann, J.-H.; Dreger, H.; Bockholt, H.; Kwade, A. Smart Electrode Processing for Battery Cost Reduction. *ECS Trans.* **2016**, *73* (1), 153–159. <https://doi.org/10.1149/07301.0153ecst>.
- (21) Hsieh, I. Y. L.; Pan, M. S.; Chiang, Y. M.; Green, W. H. Learning Only Buys You so Much: Practical Limits on Battery Price Reduction. *Appl. Energy* **2019**, *239* (August 2018), 218–224. <https://doi.org/10.1016/j.apenergy.2019.01.138>.
- (22) Bryntesen, S. N.; Strømman, A. H.; Tolstorebrov, I.; Shearing, P. R.; Lamb, J. J.; Stokke Burheim, O. Opportunities for the State-of-the-Art Production of Lib Electrodes—a Review. *Energies* **2021**, *14* (5). <https://doi.org/10.3390/en14051406>.
- (23) Jaiser, S.; Müller, M.; Baunach, M.; Bauer, W.; Scharfer, P.; Schabel, W. Investigation of Film Solidification and Binder Migration during Drying of Li-Ion Battery Anodes. *J. Power Sources* **2016**, *318*, 210–219. <https://doi.org/10.1016/j.jpowsour.2016.04.018>.
- (24) Jaiser, S.; Funk, L.; Baunach, M.; Scharfer, P.; Schabel, W. Experimental Investigation into Battery Electrode Surfaces: The Distribution of Liquid at the Surface and the Emptying of Pores

- during Drying. *J. Colloid Interface Sci.* **2017**, *494*, 22–31.
<https://doi.org/10.1016/j.jcis.2017.01.063>.
- (25) Kumberg, J.; Müller, M.; Diehm, R.; Spiegel, S.; Wachsmann, C.; Bauer, W.; Scharfer, P.; Schabel, W. Drying of Lithium-Ion Battery Anodes for Use in High-Energy Cells: Influence of Electrode Thickness on Drying Time, Adhesion, and Crack Formation. *Energy Technol.* **2019**, *7* (11), 1–11. <https://doi.org/10.1002/ente.201900722>.
- (26) Jaiser, S.; Friske, A.; Baunach, M.; Scharfer, P.; Schabel, W. Development of a Three-Stage Drying Profile Based on Characteristic Drying Stages for Lithium-Ion Battery Anodes. *Dry. Technol.* **2017**, *35* (10), 1266–1275.
<https://doi.org/https://doi.org/10.1080/07373937.2016.1248975>.
- (27) Susarla, N.; Ahmed, S.; Dees, D. W. Modeling and Analysis of Solvent Removal during Li-Ion Battery Electrode Drying. *J. Power Sources* **2018**, *378* (December 2017), 660–670.
<https://doi.org/10.1016/j.jpowsour.2018.01.007>.
- (28) Stein, M.; Mistry, A.; Mukherjee, P. P. Mechanistic Understanding of the Role of Evaporation in Electrode Processing. *J. Electrochem. Soc.* **2017**, *164* (7), A1616–A1627.
<https://doi.org/10.1149/2.1271707jes>.
- (29) Kremer, L. S.; Hoffmann, A.; Danner, T.; Hein, S.; Prifling, B.; Westhoff, D.; Dreer, C.; Latz, A.; Schmidt, V.; Wohlfahrt-Mehrens, M. Manufacturing Process for Improved Ultra-Thick Cathodes in High-Energy Lithium-Ion Batteries. *Energy Technology.* 2020.
<https://doi.org/10.1002/ente.201900167>.
- (30) Jaiser, S.; Kumberg, J.; Klaver, J.; Urai, J. L.; Schabel, W.; Schmatz, J.; Scharfer, P. Microstructure Formation of Lithium-Ion Battery Electrodes during Drying – An Ex-Situ Study Using Cryogenic Broad Ion Beam Slope-Cutting and Scanning Electron Microscopy (Cryo-BIB-SEM). *J. Power Sources* **2017**, *345*, 97–107. <https://doi.org/10.1016/j.jpowsour.2017.01.117>.

- (31) Hagiwara, H.; Suszynski, W. J.; Francis, L. F. A Raman Spectroscopic Method to Find Binder Distribution in Electrodes during Drying. *J. Coatings Technol. Res.* **2014**, *11* (1), 11–17. <https://doi.org/10.1007/s11998-013-9509-z>.
- (32) Lim, S.; Ahn, K. H.; Yamamura, M. Latex Migration in Battery Slurries during Drying. *Langmuir* **2013**, *29* (26), 8233–8244. <https://doi.org/10.1021/la4013685>.
- (33) Chen, Y. S.; Hu, C. C.; Li, Y. Y. Effects of Cathode Impedance on the Performances of Power-Oriented Lithium Ion Batteries. *J. Appl. Electrochem.* **2010**, *40* (2), 277–284. <https://doi.org/10.1007/s10800-009-9971-6>.
- (34) Westphal, B.; Bockholt, H.; Gunther, T.; Haselrieder, W.; Kwade, A. Influence of Convective Drying Parameters on Electrode Performance and Physical Electrode Properties. *ECS Trans.* **2015**, *64* (22), 57–68. <https://doi.org/10.1149/06422.0057ecst>.
- (35) Morasch, R.; Landesfeind, J.; Suthar, B.; Gasteiger, H. A. Detection of Binder Gradients Using Impedance Spectroscopy and Their Influence on the Tortuosity of Li-Ion Battery Graphite Electrodes. *J. Electrochem. Soc.* **2018**, *165* (14), A3459–A3467. <https://doi.org/10.1149/2.1021814jes>.
- (36) Sahore, R.; Wood, D. L.; Kukay, A.; Grady, K. M.; Li, J.; Belharouak, I. Towards Understanding of Cracking during Drying of Thick Aqueous-Processed LiNi_{0.8}Mn_{0.1}Co_{0.1}O₂ Cathodes. *ACS Sustain. Chem. Eng.* **2020**, *8* (8), 3162–3169. <https://doi.org/10.1021/acssuschemeng.9b06363>.
- (37) Lim, S.; Kim, S.; Ahn, K. H.; Lee, S. J. Stress Development of Li-Ion Battery Anode Slurries during the Drying Process. *Ind. Eng. Chem. Res.* **2015**, *54* (23), 6146–6155. <https://doi.org/10.1021/acs.iecr.5b00878>.
- (38) Font, F.; Protas, B.; Richardson, G.; Foster, J. M. Binder Migration during Drying of Lithium-Ion Battery Electrodes: Modelling and Comparison to Experiment. *J. Power Sources* **2018**, *393*

- (December 2017), 177–185. <https://doi.org/10.1016/j.jpowsour.2018.04.097>.
- (39) Liu, Z.; Mukherjee, P. P. Microstructure Evolution in Lithium-Ion Battery Electrode Processing. *J. Electrochem. Soc.* **2014**, *161* (8), E3248–E3258. <https://doi.org/10.1149/2.026408jes>.
- (40) Ngandjong, A. C.; Lombardo, T.; Primo, E. N.; Chouchane, M.; Shodiev, A.; Arcelus, O.; Franco, A. A. Investigating Electrode Calendering and Its Impact on Electrochemical Performance by Means of a New Discrete Element Method Model: Towards a Digital Twin of Li-Ion Battery Manufacturing. *J. Power Sources* **2021**, *485*, 229320. <https://doi.org/10.1016/j.jpowsour.2020.229320>.
- (41) Lombardo, T.; Hoock, J.; Primo, E.; Ngandjong, C.; Duquesnoy, M.; Franco, A. A. Accelerated Optimization Methods for Force-Field Parametrization in Battery Electrode Manufacturing Modeling. *Batter. Supercaps* **2020**. <https://doi.org/10.1002/batt.202000049>.
- (42) Chouchane, M.; Rucci, A.; Lombardo, T.; Ngandjong C., A.; Franco, A. A. Lithium Ion Battery Electrodes Predicted from Manufacturing Simulations: Assessing the Impact of the Carbon-Binder Spatial Location on the Electrochemical Performance. *J. Power Sources* **2019**. <https://doi.org/https://doi.org/10.1016/j.jpowsour.2019.227285>.
- (43) Shodiev, A.; Primo, E. N.; Chouchane, M.; Lombardo, T.; Ngandjong, A. C.; Rucci, A.; Franco, A. A. 4D-Resolved Physical Model for Electrochemical Impedance Spectroscopy of $\text{Li}(\text{Ni}_{1-x-y}\text{Mn}_x\text{Co}_y)\text{O}_2$ -Based Cathodes in Symmetric Cells: Consequences in Tortuosity Calculations. *J. Power Sources* **2020**, *454*, 227871. <https://doi.org/10.1016/j.jpowsour.2020.227871>.
- (44) Chouchane, M.; Primo, E. N.; Franco, A. A. Mesoscale Effects in the Extraction of the Solid-State Lithium Diffusion Coefficient Values of Battery Active Materials: Physical Insights from 3D Modeling. *J. Phys. Chem. Lett.* **2020**, *11*, 2775–2780.
- (45) Ngandjong, A. C.; Rucci, A.; Maiza, M.; Shukla, G.; Vazquez-Arenas, J.; Franco, A. A.

- Multiscale Simulation Platform Linking Lithium Ion Battery Electrode Fabrication Process with Performance at the Cell Level. *J. Phys. Chem. Lett.* **2017**, *8* (23), 5966–5972. <https://doi.org/10.1021/acs.jpcllett.7b02647>.
- (46) Srivastava, I.; Bolintineanu, D. S.; Lechman, J. B.; Scott, A. Controlling Binder Adhesion to Impact Electrode Mesostucture and Transport. *ACS Appl. Mater. Interfaces* **2020**. <https://doi.org/10.1149/osf.io/ehdq6>.
- (47) Nguyen, T. T.; Villanova, J.; Su, Z.; Tucoulou, R.; Fleutot, B.; Delobel, B.; Delacourt, C.; Demortière, A. 3D Quantification of Microstructural Properties of LiNi_{0.5}Mn_{0.3}Co_{0.2}O₂ High-Energy Density Electrodes by X-Ray Holographic Nano-Tomography. *Adv. Energy Mater.* **2021**, *2003529*, 1–15. <https://doi.org/10.1002/aenm.202003529>.
- (48) Lu, X.; Bertei, A.; Finegan, D. P.; Tan, C.; Daemi, S. R.; Weaving, J. S.; Regan, K. B. O.; Heenan, T. M. M.; Hinds, G.; Kendrick, E.; Brett, D. J. L.; Shearing, P. R. 3D Microstructure Design of Lithium-Ion Battery Electrodes Assisted by X-Ray Nano-Computed Tomography and Modelling. *Nat. Commun.* **2020**, *11* (2079), 1–13. <https://doi.org/10.1038/s41467-020-15811-x>.
- (49) Lu, X.; Daemi, S. R.; Bertei, A.; Kok, M. D. R.; O'Regan, K. B.; Rasha, L.; Park, J.; Hinds, G.; Kendrick, E.; Brett, D. J. L.; Shearing, P. R. Microstructural Evolution of Battery Electrodes During Calendering. *Joule* **2020**, *4* (12), 2746–2768. <https://doi.org/10.1016/j.joule.2020.10.010>.
- (50) Shodiev, A.; Primo, E.; Arcelus, O.; Chouchane, M.; Osenberg, M.; Hilger, A.; Manke, I.; Li, J.; Franco, A. A. Insight on Electrolyte Infiltration of Lithium Ion Battery Electrodes by Means of a New Three-Dimensional-Resolved Lattice Boltzmann Model. *Energy Storage Mater.* **2021**, *38* (January), 80–92. <https://doi.org/10.1016/j.ensm.2021.02.029>.
- (51) Xu, H.; Zhu, J.; Finegan, D. P.; Zhao, H.; Lu, X.; Li, W.; Hoffman, N.; Bertei, A.; Shearing, P.; Bazant, M. Z. Guiding the Design of Heterogeneous Electrode Microstructures for Li-Ion Batteries: Microscopic Imaging, Predictive Modeling, and Machine Learning. *Adv. Energy Mater.*

- 2021**, 2003908, 2003908. <https://doi.org/10.1002/aenm.202003908>.
- (52) Danner, T.; Singh, M.; Hein, S.; Kaiser, J.; Hahn, H.; Latz, A. Thick Electrodes for Li-Ion Batteries: A Model Based Analysis. *J. Power Sources* **2016**, *334*, 191–201. <https://doi.org/10.1016/j.jpowsour.2016.09.143>.
- (53) Jiao, K.; Leung, D. Y. C.; Xuan, J.; Leung, D. Y. C.; Xuan, J. Towards the Digitalisation of Porous Energy Materials: Evolution of Digital Approaches for Microstructural Design. *Energy Environ. Sci.* **2021**, *14*, 2549–2576. <https://doi.org/10.1039/d1ee00398d>.
- (54) Mistry, A. N.; Smith, K.; Mukherjee, P. P. Secondary-Phase Stochastics in Lithium-Ion Battery Electrodes. *ACS Appl. Mater. Interfaces* **2018**, *10* (7), 6317–6326. <https://doi.org/10.1021/acsami.7b17771>.
- (55) Laue, V.; Wolff, N.; Röder, F.; Krewer, U. Modeling the Influence of Mixing Strategies on Microstructural Properties of All-Solid-State Electrodes. *Energy Technology*. 2020. <https://doi.org/10.1002/ente.201801049>.
- (56) Pietsch, P.; Wood, V. X-Ray Tomography for Lithium Ion Battery Research: A Practical Guide. *Annu. Rev. Mater. Res.* **2017**, *47*, 451–479. <https://doi.org/10.1146/annurev-matsci-070616-123957>.
- (57) Wood, V. X-Ray Tomography for Battery Research and Development. *Nat. Rev. Mater.* **2018**, *3* (9), 293–295. <https://doi.org/10.1038/s41578-018-0053-4>.
- (58) Forouzan, M. M.; Chao, C. W.; Bustamante, D.; Mazzeo, B. A.; Wheeler, D. R. Experiment and Simulation of the Fabrication Process of Lithium-Ion Battery Cathodes for Determining Microstructure and Mechanical Properties. *J. Power Sources* **2016**, *312*, 172–183. <https://doi.org/10.1016/j.jpowsour.2016.02.014>.
- (59) Liu, C.; Arcelus, O.; Lombardo, T.; Oularbi, H.; Franco, A. A. Towards a 3D-Resolved Model of

- Si/Graphite Composite Electrodes from Manufacturing Simulations. *ChemRxiv* **2021**.
<https://doi.org/10.33774/chemrxiv-2021-9tkcd>.
- (60) Nikpour, M.; Barrett, N.; Hillman, Z.; Thompson, A. I.; Mazzeo, B. A.; Wheeler, D. R. A Model for Investigating Sources of Li-Ion Battery Electrode Heterogeneity: Part I. Electrode Drying and Calendering Processes. *J. Electrochem. Soc.* **2021**, *168* (6), 060547. <https://doi.org/10.1149/1945-7111/ac0bf1>.
- (61) <https://lammps.sandia.gov/> (Accessed on May 2021).
- (62) Chouchane, M.; Rucci, A.; Franco, A. A. A Versatile and Efficient Voxelization-Based Meshing Algorithm of Multiple Phases. *ACS Omega* **2019**, *4* (6), 11141–11144. <https://doi.org/10.1021/acsomega.9b01279>.
- (63) Joos, J.; Buchele, A.; Schmidt, A.; Weber, A.; Ivers-Tiffée, E. Virtual Electrode Design for Lithium-Ion Battery Cathodes. *Energy Technol.* **2021**, 2000891. <https://doi.org/10.1002/ente.202000891>.
- (64) Rucci, A.; Ngandjong, A. C.; Primo, E. N.; Maiza, M.; Franco, A. A. Tracking Variabilities in the Simulation of Lithium Ion Battery Electrode Fabrication and Its Impact on Electrochemical Performance. *Electrochim. Acta* **2019**, *312*, 168–178. <https://doi.org/https://doi.org/10.1016/j.electacta.2019.04.110>.
- (65) https://lammps.sandia.gov/doc/Howto_barostat.html (Accessed in May 2021).
- (66) Zielke, L.; Hutzenlaub, T.; Wheeler, D. R.; Chao, C. W.; Manke, I.; Hilger, A.; Paust, N.; Zengerle, R.; Thiele, S. Three-Phase Multiscale Modeling of a LiCoO₂ Cathode: Combining the Advantages of FIB-SEM Imaging and X-Ray Tomography. *Adv. Energy Mater.* **2015**, *5* (5), 1–8. <https://doi.org/10.1002/aenm.201401612>.
- (67) Sangrós Giménez, C.; Finke, B.; Schilde, C.; Froböse, L.; Kwade, A. Numerical Simulation of the

- Behavior of Lithium-Ion Battery Electrodes during the Calendaring Process via the Discrete Element Method. *Powder Technol.* **2019**, *349*, 1–11. <https://doi.org/10.1016/j.powtec.2019.03.020>.
- (68) Chen, H.; Ling, M.; Hencz, L.; Ling, H. Y.; Li, G.; Lin, Z.; Liu, G.; Zhang, S. Exploring Chemical, Mechanical, and Electrical Functionalities of Binders for Advanced Energy-Storage Devices. *Chem. Rev.* **2018**, *118* (18), 8936–8982. <https://doi.org/10.1021/acs.chemrev.8b00241>.
- (69) <https://github.com/ARTISTIC-ERC/Manufacturing-Model-Codes> (accessed on June 2021).
- (70) <https://www.erc-artistic.eu/computational-portal> (Accessed on June 2021).